Environmental Research Letters



OPEN ACCESS

RECEIVED

9 December 2018

REVISED

18 March 2019

ACCEPTED FOR PUBLICATION
22 March 2019

PUBLISHED

17 May 2019

Original content from this work may be used under the terms of the Creative Commons Attribution 3.0 licence.

Any further distribution of this work must maintain attribution to the author(s) and the title of the work, journal citation and DOI



LETTER

Ocean warming pattern effects on future changes in East Asian atmospheric rivers

Youichi Kamae 100, Wei Mei2 and Shang-Ping Xie3

- ¹ Faculty of Life and Environmental Sciences, University of Tsukuba, Tsukuba, Japan
- ² Department of Marine Sciences, University of North Carolina at Chapel Hill, Chapel Hill, NC, United States of America
- ³ Scripps Institution of Oceanography, University of California San Diego, La Jolla, CA, United States of America

E-mail: kamae.yoichi.fw@u.tsukuba.ac.jp

Keywords: heavy rainfall, atmospheric river, ENSO, the North Pacific high, Indian Ocean capacitor Supplementary material for this article is available online

Abstract

Atmospheric rivers (ARs), intense water vapor transports associated with extra-tropical cyclones, frequently bring heavy rainfalls over mid-latitudes. Over East Asia, landfalling ARs result in major socio-economic impacts including widespread floods and landslides; for example, western Japan heavy rainfall in July 2018 killed more than 200 people. Using results of high-resolution atmospheric model ensemble simulations, we examine projected future change in summertime AR frequency over East Asia. Different sea surface temperature (SST) warming patterns derived from six atmosphere—ocean coupled model simulations were assumed to represent uncertainty in future SST projections. The rate of increase in the frequency of landfalling ARs over summertime East Asia is on average 0.9% K⁻¹ and is dependent on SST warming patterns. Stronger warming over the North Indian Ocean and South China Sea or weaker warming over the tropical central Pacific produce more frequent landfalling ARs over East Asia. These patterns are similar to the co-variability of SST, atmospheric circulation, and ARs over the western North Pacific found on the interannual time scale. The results of this study suggest that the natural disaster risk related to landfalling ARs should increase over East Asia under global warming and SSTs over the Indo-Pacific region holds the key for a quantitative projection.

1. Introduction

Atmospheric rivers (ARs), narrow corridors of enhanced moisture transport extending for thousands of kilometers, often cause natural disasters over the middle latitudes including East Asia (e.g. Lavers and Villarini 2013, Neiman et al 2013, Gimeno et al 2016, Kamae et al 2017c, Waliser and Guan 2017). For example, an AR-like enhanced water vapor transport was closely related to occurrence of the heavy rain event of July 2018 in Japan that caused 221 fatalities due to widespread floods and landslides (Tsuguti et al 2019). Many previous studies have been devoted to investigating future change in AR activity because it is the key for projecting water resources and natural disaster risk. Increased water vapor transports associated with ARs are robustly projected (Lavers et al 2013, Payne and Magnusdottir 2015, Gao et al 2015,

Warner *et al* 2015, Espinoza *et al* 2018) because of atmospheric water vapor increase in response to global warming (O'Gorman *et al* 2012 and references therein). In addition to this thermodynamic effect, future change in atmospheric circulation (dynamic effect; e.g. Ma and Xie 2013, Shepherd 2014) is important for projecting regional changes in AR activity (Payne and Magnusdottir 2015, Gao *et al* 2015, 2016, Shields and Kiehl 2016, Espinoza *et al* 2018).

Previous works examined projected future changes in AR activity based on multi-model outputs from the Coupled Model Intercomparison Project phase 5 (CMIP5; Taylor *et al* 2012). Regional projections of AR frequency in a warming world exhibit large spreads among models (Payne and Magnusdottir 2015, Guan and Waliser 2017, Espinoza *et al* 2018). Some of the models have limited skill in representing current AR



behavior and its statistics (frequency, intensity, and variability), limiting reliability of AR projections using such models (Payne and Magnusdottir 2015, Guan and Waliser 2017). In general, higher resolution is necessary to represent more realistic structure (and statistics) of ARs (models with horizontal resolution of 0.7°-1.3° have generally higher skills than models with 1.9°-3.7°; figure 2 of Payne and Magnusdottir 2015) because they are transient and synoptic-scale phenomena (Wick et al 2013, Hagos et al 2015, Guan and Waliser 2017). Furthermore, it is also important to understand effect of internal variability from derived statistics of model outputs (e.g. Hawkins and Sutton 2009, Thompson et al 2015) by using large-member ensemble simulations (e.g. Deser et al 2012, Hagos et al 2016, Kamae et al 2017a, 2017b) for quantitative evaluation of forced response to global warming.

Another important source of uncertainty in climate projections is sea surface temperature (SST) warming pattern (e.g. Mizuta et al 2014, Xie et al 2015), which is important for projecting North-Pacific atmospheric circulation (e.g. Shin and Sardeshmukh 2011, Ma and Xie 2013, Shepherd 2014, He and Zhou 2015, Choi et al 2016) and statistics of extratropical cyclones (Langenbrunner et al 2015). SST anomalies over the tropical Indo-Pacific regions are also closely linked to interannual variability in atmospheric circulation over Asia and the western North Pacific (Xie et al 2009, Wang et al 2013, Song and Zhou 2014a, 2014b, Kamae et al 2017b, Paek et al 2018). However, it is not easy to evaluate the effect of SST warming pattern uncertainty, because other factors (e.g. model resolution, physics, and biases) also affect the results obtained from the CMIP multiple model ensemble.

In this study, we employ ensemble simulations by a high-resolution atmospheric general circulation model (AGCM) to evaluate the dynamic component of uncertainties in projected AR changes, which is primarily related to the effect of SST pattern. The model shows skills in reproducing climatology and variability of AR activity over the northwestern Pacific, and was forced by different SST warming patterns.

2. Data and method

2.1. AGCM and current climate simulation

We examine large-ensemble simulation outputs called d4PDF (Mizuta *et al* 2017) developed using the Meteorological Research Institute Atmospheric General Circulation Model (MRI-AGCM) version 3.2 (Mizuta *et al* 2012). Mizuta *et al* (2017) provided details of the model and experiments. Horizontal resolution of this AGCM is TL319 (equivalent to 60 km grid). The number of vertical level is 64 (with the top at 0.01 hPa). To conduct current climate simulation for 1951–2010, the model was forced by observed SST, sea ice (Hirahara *et al* 2014), and historical radiative forcing

agents (greenhouse gases, aerosols, and ozone). The ensemble simulations were developed with random initial and SST perturbations (Hirahara *et al* 2014). In this study, a 10-member ensemble mean was examined to reduce the effect of atmospheric internal variability (Kamae *et al* 2017a, 2017b).

We detect ARs using a methodology modified from Mundhenk et al (2016). First, vertically integrated water vapor transport (IVT) is calculated using 6-hr atmospheric variables. IVT anomaly is calculated by comparing with its climatology. Next, shape (e.g. length > 1500 km, area $> 7.8 \times 10^5$ km², lengthwidth ratio > 1.325) and intensity (140 kg m⁻¹ s⁻¹) of anomalous IVT are checked to detect ARs. The detection scheme can filter out circular IVT anomalies associated with tropical cyclones via the shape criterion (see figure A2 of Mundhenk et al 2016). Note that ARlike IVT anomalies examined in this study are sometimes influenced by remote effects of tropical cyclone (Kamae et al 2017c). AR frequency examined in this study is defined as the fraction of time periods during which an AR exists to the total number of periods. Kamae et al (2017b) reported that this model can realistically simulate the climatology, seasonal cycle, and interannual variability of North-Pacific AR compared to an atmospheric reanalysis.

2.2. Future projection

In addition to the current climate simulation, outputs from global warming simulations (Mizuta et al 2017) were also examined to evaluate future change in AR activity. In this set of simulations, the model was forced by constant radiative forcing, SST warming patterns, and anomalous sea ice concentration. Anomalous radiative forcing corresponding to the level of year 2090 in the Representative Concentration Pathway (RCP) 8.5 scenario adopted in CMIP5 was added to the radiative forcing in the current climate simulation. Six SST warming patterns derived from cluster analyses of CMIP5 multi-model results (figure S1 is available online: stacks.iop.org/ERL/14/054019/ mmedia; Mizuta et al 2014) were added to historical SST. The six SST warming patterns were based on RCP8.5 simulations by CCSM4 (hereafter CC), GFDL-CM3 (GF), HadGEM2-AO (HA), MIROC5 (MI), MPI-ESM-MR (MP), and MRI-CGCM3 (MR). Each SST warming pattern was scaled so that the simulated global-mean surface air warming from the pre-industrial level is equal to 4 K (Mizuta et al 2017). The six patterns exhibit different zonal and meridional gradients over the Pacific, Indian and Atlantic Oceans (table S1, figure S1). For example, CC run was forced by La Niña-like SST pattern in the tropical Pacific (larger warming over the western equatorial Pacific than central-to-eastern equatorial Pacific), in contrast to El Niño-like warming pattern prescribed in other runs (figure S1; see section 3.3). Among the six runs, tropical Atlantic warming and meridional warming



contrast between 30°-60°N and EQ-30°N in the North Pacific are strongest in MI and GF runs, respectively (table S1, figures S1, S2). In each run, ensemble was developed in a similar way to the current climate simulation (section 2.1). The AR detection scheme described in section 2.1 and used in Kamae *et al* (2017b) was applied to the outputs of global warming simulation.

To evaluate the forced response to radiative forcing and SST warming, 10-member ensemble mean, 60-yr climatology of AR frequency in each run is compared. In this study, projected changes between global warming and current climate simulations scaled by tropical-mean (30°S–30°N) SST anomaly are represented as $\Delta (K^{-1})$. Average of Δ among six warming simulations can be regarded as a robust response to global warming simulated in this model. Deviations of Δ in individual warming simulations from the averaged Δ can be considered as the effect of Δ SST deviation from the averaged warming pattern (figure S2).

3. Results

3.1. AR response to climate warming

We first examine simulated changes in atmospheric circulation and AR frequency in each season robustly found among the six warming simulations. Figure 1 shows six-run-mean sea level pressure (SLP) response (Δ SLP), change in AR frequency, and prescribed Δ SST. Averaged Δ SST pattern is almost identical to the ensemble mean of CMIP models: stronger warming over the mid- and high-latitude North Pacific than the tropics, and stronger warming over the tropical eastern Pacific than western Pacific (e.g. Xie et al 2010, Mizuta et al 2014). During boreal summer, the North Pacific High (NPH) weakens (negative Δ SLP) in response to climate warming (figure 1(e); table 1), consistent with CMIP5 ensemble mean response reported in previous studies (He et al 2017, Song et al 2018). In this model, the western North Pacific subtropical high (WNPSH) around the Philippines is enhanced (figure 1(e); table 1), although model responses are divergent among CMIP5 models (He and Zhou 2015). Despite seasonal variations in Δ SLP and associated low-level circulation response (figures 1(a), (c), (e), (g)), AR frequency is increased over the middle and high latitudes during almost all the seasons (figures 1(b), (d), (f), (h)). The general increasing trend of ARs under climate warming can be attributed to thermodynamic effect (e.g. Lavers et al 2013, Gao et al 2015). Atmospheric water vapor increase and resultant positive ΔIVT should result in more AR count because the anomalous IVT threshold (section 2.1) is identical between current climate and global warming simulations.

ARs become more frequent over East Asia (0.91 \pm 0.15 % K⁻¹; table 1), western North America, eastern North America, and Europe (figures 1(b), (d),

(f), (h)). During boreal summer, large increases in AR frequency over the subtropical North Pacific and East Asia (25°-40°N) are concurrent with anomalous lowlevel circulations associated with the weakened NPH and the enhanced WNPSH. Anomalous moist southwesterlies on the southeastern flank of the weakened NPH and on the northwestern flank of the enhanced WNPSH increase AR occurrences over those regions (figure 1(e); detailed in section 3.2). Such circulation-AR relationship is consistent with what found in interannual variability (Kamae et al 2017b; detailed in section 3.3). Such a dynamic effect of atmospheric circulation on regional changes in AR frequency (e.g. Payne and Magnusdottir 2015, Shields and Kiehl 2016; see section 1) suggests the importance of \triangle SST pattern in future projections of North-Pacific AR activity. In this study, we mainly focus on North-Pacific ARs during boreal summer. AR responses during other seasons and over other regions will be examined in future studies.

3.2. Uncertainty related to tropical SST warming pattern

Next, we examine sensitivity to \triangle SST pattern. Figure 2 shows changes in boreal summer AR frequency over East Asia and the North Pacific simulated in the six runs. All the simulations produce a general increase in North-Pacific AR frequency, but the circulation and AR responses exhibit large spreads among the six runs: limited enhancement of WNPSH (limited weakening of NPH) in CC, GF, MP and MR runs (CC run) compared to other runs (table 1). The differences in the quantitative changes in East-Asian ARs (table 1) are partly related to the spreads of the WNPSH response. For example, MI run shows the largest enhancement of WNPSH among the six runs and correspondingly the largest increase in East-Asian AR occurrence (table 1) especially over southeastern China (figure 2(d)), while the changes are relatively weak in GF and MP runs (table 1, figures 2(b), (e), S3). These results suggest that a significant portion of the uncertainty in ΔARs is due to the SST-mediated dynamic effect (see section 3.3).

However, the WNPSH response cannot explain all the spreads of East Asian \triangle ARs. For example, CC run (figure 2(a)) produces larger East-Asian \triangle ARs than GF, HA, MP and MR runs (table 1) but not a larger enhancement of WNPSH. Another feature found in CC run is a limited weakening of NPH and associated North-Pacific circulation response (figure S3). Here circulation anomaly associated with NPH response is important for $\triangle AR$ pattern over the North Pacific. GF run shows the largest weakening of NPH, causing a southeastward shift of seasonal-mean AR frequency over the North Pacific: a moderate increase over the middle latitudes on the northwestern flank of the anomalous NPH with a greater increase over the subtropics on the southeastern flank



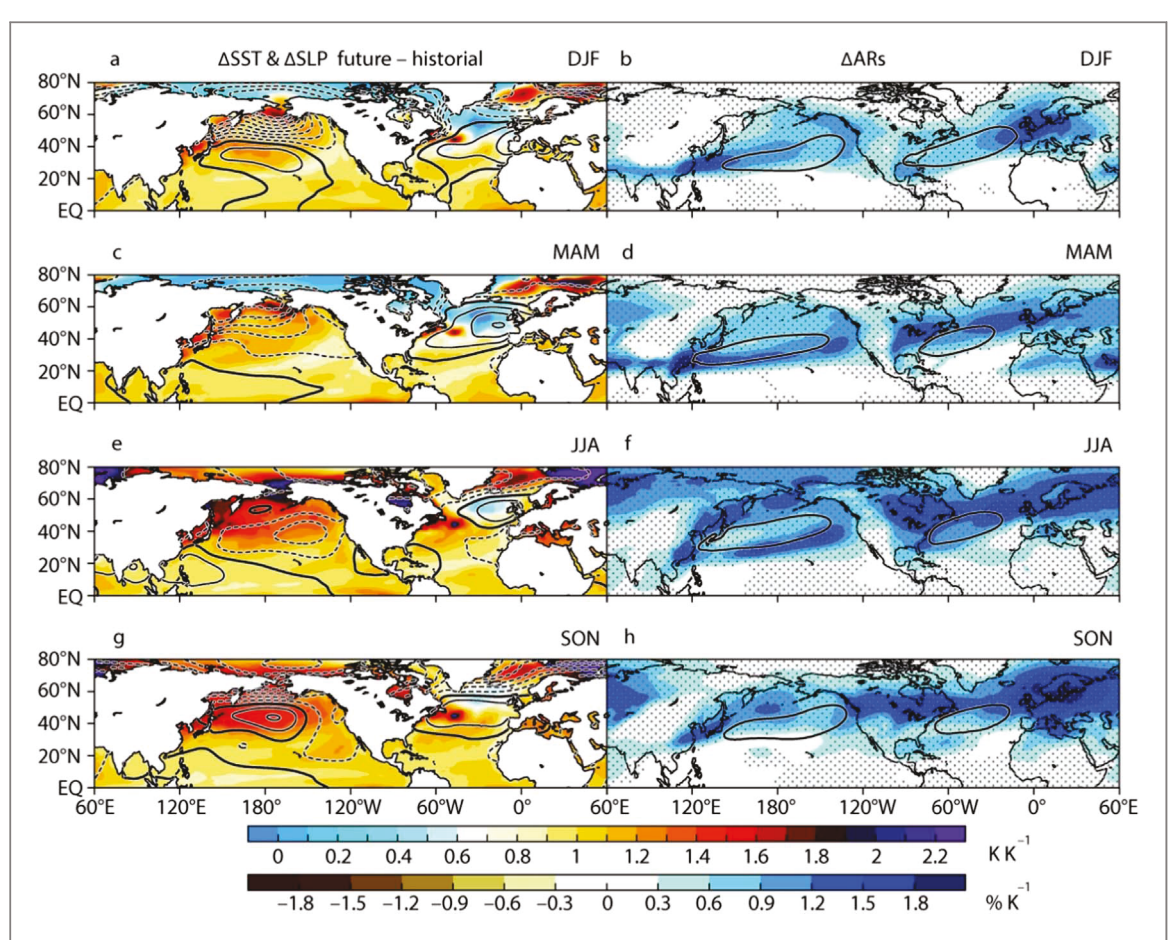


Figure 1. Ensemble mean responses of sea level pressure (Δ SLP) and frequency of atmospheric rivers (Δ ARs) over the Northern Hemisphere to climate warming (future minus current) simulated in d4PDF. All the results are scaled by tropical-mean (30°S–30°N) sea surface temperature increase (Δ SST; K). (a), (c), (e), (g) Prescribed Δ SST pattern (K K⁻¹; shading) and simulated Δ SLP (contours). Thick contours indicate Δ SLP of 0. Solid and dashed contours indicate positive and negative Δ SLP (contour interval is 0.25 hPa K⁻¹). (b), (d), (f), (h) Δ ARs (% K⁻¹; shading) and climatological ARs of 14% (contours). Stipples indicate the areas with 95% statistical confidence in Δ ARs. (a), (b) December-to-February (DJF), (c), (d) March-to-May (MAM), (e), (f) June-to-August (JJA), and (g), (h) September-to-November (SON).

Table 1. Simulated changes in sea level pressure (Δ SLP; hPa K⁻¹) averaged over the North Pacific High (NPH) region ($25^{\circ}-45^{\circ}$ N, $180^{\circ}-130^{\circ}$ W) and the western North Pacific subtropical high (WNPSH) region ($10^{\circ}-25^{\circ}$ N, $110^{\circ}-130^{\circ}$ E) and frequency of atmospheric rivers (Δ ARs; % K⁻¹) averaged over the East Asian region ($20^{\circ}-45^{\circ}$ N, $100^{\circ}-150^{\circ}$ E; figure 2) under global warming in each experiment. Uncertainty range represents ± 1 standard deviation among 10-member ensemble simulations. Bottom low indicates ensemble mean and ± 1 standard deviation of the six simulations (60 members).

Experiments	NPH Δ SLP (hPa K ⁻¹)	WNPSH Δ SLP (hPa K ⁻¹)	East Asian ΔARs (% K ⁻¹)
CC	-0.26 ± 0.05	0.21 ± 0.03	1.01 ± 0.05
GF	-0.66 ± 0.04	0.34 ± 0.03	0.86 ± 0.06
HA	-0.55 ± 0.06	0.44 ± 0.03	0.88 ± 0.06
MI	-0.56 ± 0.05	0.78 ± 0.01	1.14 ± 0.07
MP	-0.39 ± 0.05	0.36 ± 0.03	0.70 ± 0.06
MR	-0.44 ± 0.03	0.34 ± 0.03	0.91 ± 0.06
All	-0.48 ± 0.14	$\boldsymbol{0.39 \pm 0.19}$	$\boldsymbol{0.91 \pm 0.15}$

(figure 2(b)). Such a meridional shift is not apparent in CC run (figure 2(a)), suggesting that the NPH response is also an important factor for the spatial pattern of ΔARs over the North Pacific.

The spreads in circulation and AR responses result from differences in Δ SST prescribed in these runs. Here SST-circulation-AR relationship found in the global warming simulations appears consistent with that observed in interannual variability. In the next

subsection, we examine the relationship found in interannual variability and compare it with the results shown above.

${\bf 3.3.}\,Comparison\,with\,interannual\,variability$

Figure 3 shows major modes of interannual variability of East-Asian summertime ARs in the current climate simulation for 1951–2010 based on empirical orthogonal function (EOF) analysis of 10-member ensemble



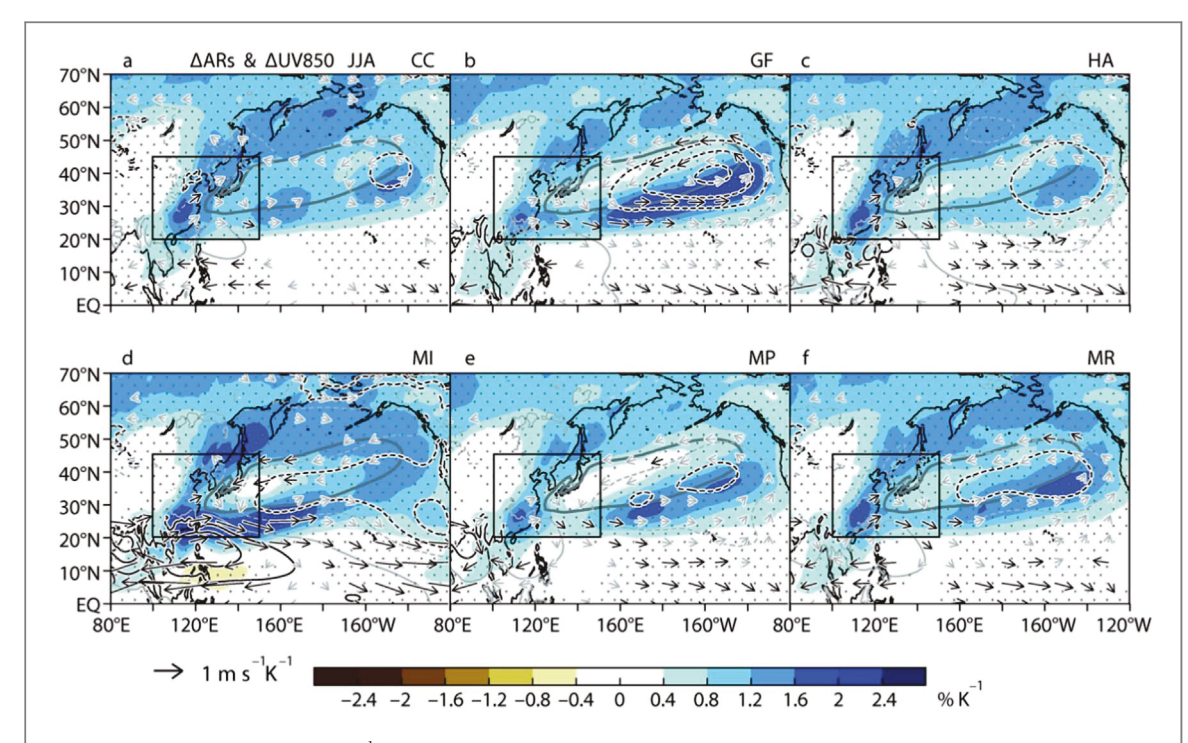


Figure 2. Boreal summer Δ ARs (% K^{-1} ; shading) simulated in six warming runs. (a) CC, (b) GF, (c) HA, (d) MI, (e) MP and (f) MR runs. Stipples indicate the areas with 95% statistical confidence. Solid and dashed contours indicate positive and negative Δ SLP (grey: \pm 0.25 hPa K^{-1} , black: \pm 0.5, 0.75 and 1 hPa K^{-1}). Thick grey contours indicate climatological ARs of 14%. Vectors represent response of horizontal wind at the 850 hPa level (Δ UV850; m s⁻¹ K^{-1}). Rectangle indicates the East-Asian region examined in table 1 and figure 4.

mean. Note that EOF1 is nearly identical to the ENSOrelated interannual variability in reanalysis and d4PDF (Kamae et al 2017b). The EOF1 is modulated by the Indo-western Pacific Ocean capacitor effect (IPOC; Xie et al 2016): eastward propagating Kelvin waves and an anomalous WNPSH (figure 3(a)) induced by the North Indian Ocean (NIO) and the South China Sea warming after wintertime El Niño development (figure 3(c); Xie et al 2009). Note that warm SST anomaly over the equatorial Pacific (5° S–5°N, 170°– 120°W) associated with EOF1 rapidly diminishes after the wintertime El Niño peak, resulting in very modest anomaly during summer (figure 3(c); see figure 8 of Kamae et al 2017b). The strengthened southwesterlies on the northwestern flank of the WNPSH increase AR occurrence over East Asia (figure 3(a); Kamae et al 2017b). Here the meridional atmospheric teleconnection (Pacific-Japan pattern) associated with IPOC (Xie et al 2016) results in a pair of anticyclone and cyclone over the subtropical western North Pacific and over Okhotsk Sea, producing a tripolar pattern of AR anomalies, as reported in Kamae et al (2017b).

In contrast to the tripolar pattern, the EOF2 is characterized by a dipole pattern of AR frequency over the North Pacific: an increase over the extratropics and a decrease over the subtropics (figure 3(b)). Atmospheric circulation associated with EOF2 exhibits an anticyclonic anomaly over the North Pacific, indicating an enhanced NPH. The circulation-AR relationship, an increase (decrease) in ARs on the northwestern (southeastern) flank of the anomalous

anticyclone, is similar to that in EOF1 although positions and horizontal extent are different. The anomalous circulation (figure 3(b)) facilitates more frequent landfalling ARs over East Asia (especially northeastern China, Korean Peninsula, and northern Japan) and suppresses ARs off the Pacific coasts of Japan. Figure 3(d) shows the anomalous SST pattern corresponding to EOF2. Negative SST anomalies are found over the central and eastern tropical Pacific, indicating a summertime development of La Niña. The relationship between summertime SST anomaly and the NPH is consistent with previous studies (e.g. Wang et al 2013, Paek et al 2018). Details of La Niña-induced anomalies in atmospheric circulation and ARs over the North Pacific are currently being extensively examined and will be reported in a separated paper.

The SST-circulation-AR relationship found here is helpful for detecting the SST pattern effect on North-Pacific Δ ARs under global warming. The SST forcing prescribed in MI run exhibits larger warming over the NIO and the South China Sea and weaker warming over the central equatorial Pacific than the six-run mean (table S1, figures 4, S1, S2). The larger enhancement of WNPSH under global warming in MI run is consistent with CMIP5 inter-model spreads (He and Zhou 2015) and the SST-circulation relationship found in interannual variability (figure 3). CC run was forced by La Niña-like Δ SST pattern (zonal Δ SST gradient between the western equatorial Pacific and central equatorial Pacific; table S1, figures S1, S2), in contrast to El Niño-like Pacific Δ SST found in the

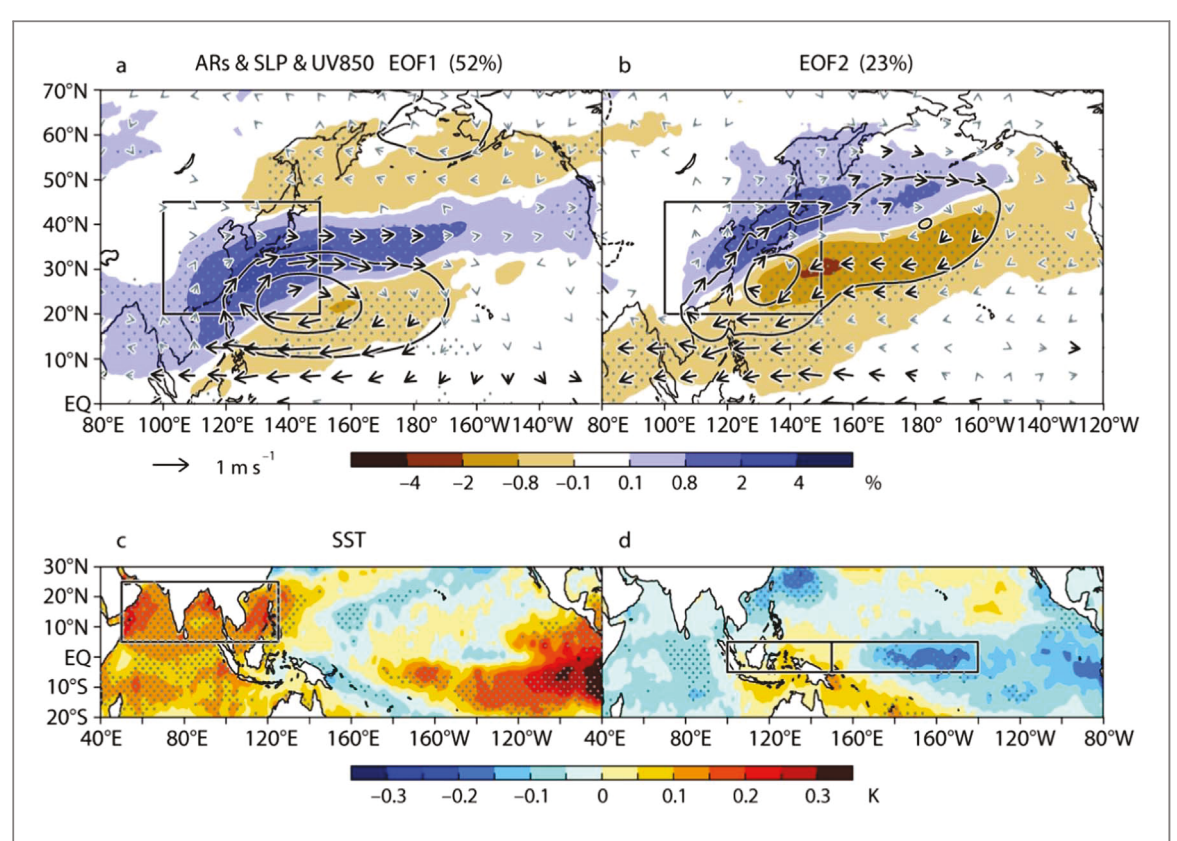


Figure 3. The first and second modes of interannual variation of ARs (%) over the East-Asian region $(20^\circ-45^\circ\text{N}, 100^\circ-150^\circ\text{E})$ during JJA in d4PDF current climate simulations for 1951–2010. Linear trends were removed from all variables before the analyses. (a), (c) The first mode of empirical orthogonal function (EOF1; 52%) and (b), (d) the second mode (EOF2; 23%). Shadings represent regressions of ARs onto time series of principal components (PCs). Solid and dashed contours in (a), (b) indicate positive and negative values of regressed SLP (± 0.2 and 0.5 hPa) onto PCs. Vectors indicate regressed UV850 (m s⁻¹). (c), (d) Regressed SST (K). Stippling indicates the area with 95% statistical confidence of (a), (b) ARs and (c), (d) SST. Rectangles in (c) and (d) indicate regions examined in figure 4.

multi-model ensemble mean (e.g. Xie et al 2010, Mizuta et al 2014). The Δ SST in CC run is consistent with the weak NPH response compared to other runs (table 1, figures 2(a), S3(a)). These results suggest that the anomalous NIO and South China Sea warming and La Niña-like SST gradient are important factors for the inter-model spreads in Δ ARs over East Asia and the North Pacific. Note that Δ SST over other regions including the Atlantic Ocean (table S1, figures S1, 2) may also play some roles (e.g. Chen et al 2014, Hong et al 2014), which is not discussed here since our focus in this study is on the tropical Indian and Pacific Ocean.

Figure 4(a) shows the interannual relationship among NIO SST (averaged over $50^{\circ}-125^{\circ}E$, $5^{\circ}-25^{\circ}N$), zonal SST gradient between the tropical western Pacific (TWP) and tropical central Pacific (TCP; $100^{\circ}-150^{\circ}E$, $5\,S^{\circ}-5^{\circ}N$ minus $150E^{\circ}-140^{\circ}W$, $5\,S^{\circ}-5^{\circ}N$), and East-Asian summertime AR frequency for 1951-2010. Removing linear trends for 1951-2010 from these variables does not change the results significantly. Here the two SST indices are not significantly correlated (r=0.07). If we use these two as explanatory variables, East Asian ARs (%) can be approximated using a multiple linear regression ($R^2=0.57$) as follows:

$$ARs = -83.79 + 3.23X_1 + 0.39X_2, \tag{1}$$

where X_1 is NIO SST (°C) and X_2 is TWP SST minus TCP SST (K). Years with higher NIO SST tend to produce more frequent East Asian ARs as reported in Kamae et al (2017b). In addition, warmer TWP than TCP (La Niña-like SST gradient) is associated with increased East Asian ARs. Similarly, SSTs in these two regions are important for the spreads of East-Asian Δ ARs among the six warming simulations. Figure 4(b) shows relationship between NIO Δ SST, TWP Δ SST minus TCP Δ SST, and East Asian Δ ARs in these runs. As a reference, we also plot Δ SST simulated in CMIP5 models (Taylor et al 2012; table S2). The six d4PDF runs effectively cover uncertainty ranges of the tropical Δ SST pattern in CMIP5 models (Mizuta et al 2014) except two models (strong La Niña-like SST gradient simulated in FGOALS-g2 and weak NIO warming in INMCM4). The East Asian Δ ARs is approximated as follows:

$$\Delta ARs = -0.82 + 1.66X_1 + 0.94X_2,$$
 (2)

where X_1 is NIO Δ SST (K) and X_2 is TWP Δ SST minus TCP Δ SST (K). R^2 of equation (2) is 0.66. Among the d4PDF runs, the larger increases in SST over the NIO and the South China Sea in MI and MR runs (table S1, figure 4(b), S2) are associated with larger increases in East-Asian Δ ARs (table 1, figures 2, 4(b)). In addition, the La Niña-like Δ SST gradients in



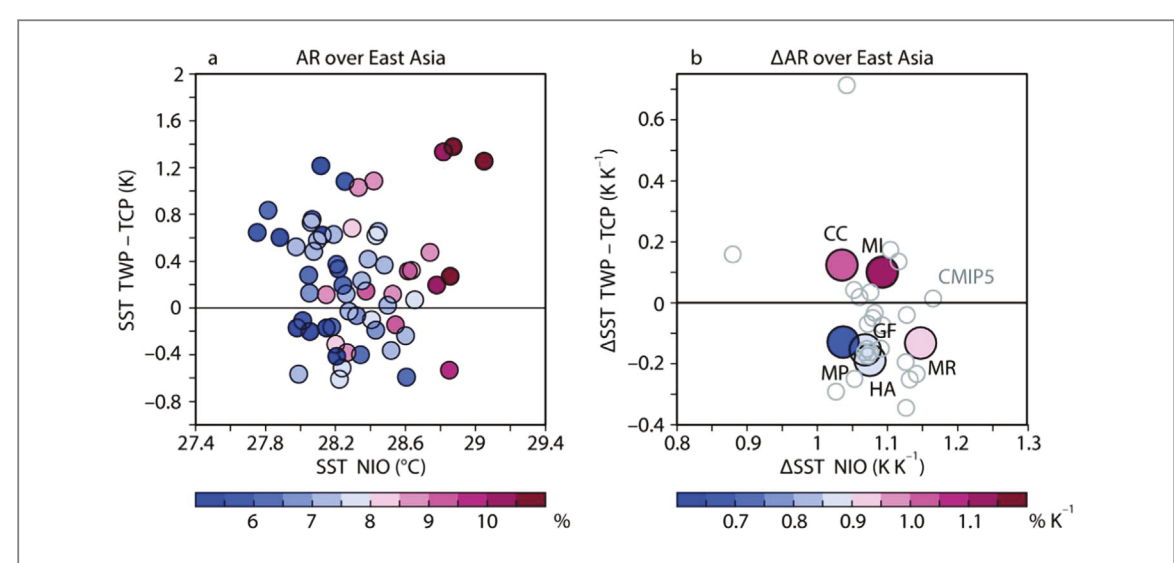


Figure 4. Relationship between SST and East Asian ARs during JJA. (a) Interannual variations of NIO SST ($50^{\circ}-125^{\circ}\text{E}$, $5^{\circ}-25^{\circ}\text{N}$); °C; horizontal axis), SST difference between tropical western Pacific (TWP; $100^{\circ}-150^{\circ}\text{E}$, $58^{\circ}-5^{\circ}\text{N}$) and tropical central Pacific (TCP; 150E°- 140°W , $58^{\circ}-5^{\circ}\text{N}$; K; vertical axis), and 10-member ensemble mean frequency of East Asian ARs (%; colors) in the current climate simulation for 1951-2010. (b) NIO Δ SST (K K $^{-1}$), TWP Δ SST minus TCP Δ SST (K K $^{-1}$), and East Asian Δ ARs (% K $^{-1}$) simulated in d4PDF six warming runs. Grey circles indicate Δ SST (difference in 30 year climatology between representation concentration pathway 4.5 run for 2071–2100 and historical simulation for 1979–2008) simulated in 24 CMIP5 models (table S2).

CC and MI runs (figure 4(b), S2) are also related to greater increases in East-Asian \triangle ARs (table 1, figures 2, 4(b)). Based on these results, we suggest that the two \triangle SST indices are important sources of uncertainty in East-Asian \triangle ARs. Note that the regression coefficients obtained in equation (2) based on the limited samples size (n=6) may be sensitive to increasing sample size. Relative importance of NIO SST (X_1) compared to the zonal SST gradient (X_2) under global warming should be further tested using sensitivity experiments prescribed with idealized SST warming patterns.

4. Summary and discussion

Future changes in AR activity over East Asia and the North Pacific and their uncertainty related to SST warming pattern are investigated using large ensemble simulations by a high-resolution AGCM. Generally, ARs become more frequent over the Northern Hemisphere including summertime East Asia due to increased water vapor in a warming climate. In addition to the robust thermodynamic effect, dynamic effect is important for the spreads of East-Asian \triangle ARs among different SST warming experiments via changing atmospheric circulation patterns over the Indo-Pacific region. A warmer NIO-South China Sea results in an enhanced WNPSH, and the strengthened moist southwesterlies increase AR occurrence on the northwestern flank. In addition, La Niña-like tropical Pacific SST gradient is important for the NPH response and a resultant increase in East-Asian ARs. These SSTcirculation-AR relationships are similar to those found in interannual variability. Our results suggest that the tropical Δ SST patterns are important sources of uncertainty in future projections of natural disaster risk via ARs over summertime East Asia.

The investigation based on a single climate model enables us to examine effects of imposed forcing (e.g. Δ SST pattern) on ARs. However, the uncertainty range is not necessarily covered by the single-AGCM experiments even though imposed ΔSST sufficiently covers the spreads of Δ SST projected by different models. In addition, the quantitative results obtained in this study are possibly dependent on choices of thresholds employed in the AR detection (e.g. IVT threshold; Guan and Waliser 2015, Shields et al 2018). Recently, intercomparison projects on high-resolution climate models (Haarsma et al 2018) and on AR detection methods (Shields et al 2018) are proposed for comprehensive evaluation of uncertainties rooted from climate models and AR detection methods. Further research is needed to evaluate robustness of the results obtained in this study. This study only focuses on summertime AR activity over East Asia and the North Pacific. Robust and uncertain parts of future projections of AR activity during other seasons and over other regions are also worth examining in future studies.

Acknowledgments

This work was supported by JSPS KAKENHI Grant Number 17K14388 and the Integrated Research Program for Advancing Climate Models (TOUGOU program) from the Ministry of Education, Culture, Sports, Science and Technology (MEXT), Japan. The d4PDF dataset is available via DIAS website (http://search.diasjp.net/en/dataset/d4PDF_GCM). We thank two anonymous reviewers for their constructive comments on this manuscript.



ORCID iDs

Youichi Kamae https://orcid.org/0000-0003-0461-5718

References

- Chen W, Lu R and Dong B 2014 Intensified anticyclonic anomaly over the western North Pacific during El Niño decaying summer under a weakened Atlantic thermohaline circulation *J. Geophys. Res. Atmos.* 119 13637–50
- Choi J, Lu J, Son S-W, Frierson D M W and Yoon J-H 2016 Uncertainty in future projections of the North Pacific subtropical high and its implication for California winter precipitation change J. Geophys. Res. Atmos. 121 795–806
- Deser C, Knutti R, Solomon S and Phillips A S 2012 Communication of the role of natural variability in future North American climate *Nat. Clim. Change* 2 775–9
- Espinoza V, Waliser D E, Guan B, Lavers D A and Ralph F M 2018 Global analysis of climate change projection effects on atmospheric rivers *Geophys. Res. Lett.* **45** 4299–308
- Gao Y, Lu J, Leung L R, Yang Q, Hagos S and Qian Y 2015 Dynamical and thermodynamical modulations on future changes of landfalling atmospheric rivers over western North America Geophys. Res. Lett. 42 7179–86
- Gao Y, Lu J and Leung L R 2016 Uncertainties in projecting future changes in atmospheric rivers and their impacts on heavy precipitation over Europe J. Clim. 29 6711–26
- Gimeno L, Dominguez F, Nieto R, Trigo R, Drumond A, Reason C J C, Taschetto A S, Ramos A M, Kumar R and Marengo J 2016 Major mechanisms of atmospheric moisture transport and their role in extreme precipitation events *Ann*. *Rev. Environ. Res.* 41 117–41
- Guan B and Waliser D E 2017 Atmospheric rivers in 20 year weather and climate simulations: a multimodel, global evaluation *J. Geophys. Res. Atmos.* 122 5556–81
- Haarsma R J et al 2018 High resolution model intercomparison project (HighResMIP v1.0) for CMIP6 Geosci. Model Dev. 9 4185–208
- Hagos S, Leung L R, Yang Q, Zhao C and Lu J 2015 Resolution and dynamical core dependence of atmospheric river frequency in global model simulations J. Clim. 28 2764–76
- Hagos S M, Leung L R, Yoon J-H, Lu J and Gao Y 2016 A projection of changes in landfalling atmospheric river frequency and extreme precipitation over western North America from the Large Ensemble CESM simulations *Geophys. Res. Lett.* 43 1357–63
- Hawkins E and Sutton R 2009 The potential to narrow uncertainty in regional climate predictions *Bull. Am. Meteorol. Soc.* **90** 1095–107
- He C and Zhou T 2015 Responses of the western North Pacific subtropical high to global warming under RCP4.5 and RCP8.5 scenarios projected by 33 CMIP5 models: the dominance of tropical Indian Ocean–tropical western Pacific SST gradient J. Clim. 28 365–80
- He C, Wu B, Zou L and Zhou T 2017 Responses of the summertime subtropical anticyclone to global warming *J. Clim.* **30** 6465–79
- Hirahara S, Ishii M and Fukuda Y 2014 Centennial-scale sea surface temperature analysis and its uncertainty *J. Clim.* **27** 57–75
- Hong C C, Chang T C and Hsu H H 2014 Enhanced relationship between the tropical Atlantic SST and the summertime western North Pacific subtropical high after the early 1980s J. Geophys. Res. Atmos. 119 3715–22
- Kamae Y *et al* 2017a Forced response and internal variability of summer climate over western North America *Clim. Dyn.* **49**
- Kamae Y, Mei W, Xie S-P, Naoi M and Ueda H 2017b Atmospheric rivers over the Northwestern Pacific: climatology and interannual variability *J. Clim.* **30** 5605–19

- Kamae Y, Mei W and Xie S-P 2017c Climatological relationship between warm season atmospheric rivers and heavy rainfall over East Asia J. Meteorol. Soc. Japan 95 411–31
- Langenbrunner B, Neelin J D, Lintner B R and Anderson B T 2015
 Patterns of precipitation change and climatological
 uncertainty among CMIP5 models, with a focus on the
 midlatitude Pacific storm track *J. Clim.* 28 7857–72
- Lavers D A and Villarini G 2013 The nexus between atmospheric rivers and extreme precipitation across Europe *Geophys. Res. Lett.* 40 3259–64
- Lavers D A, Allan R P, Villarini G, Lloyd-Hughes B, Brayshaw D J and Wade A J 2013 Future changes in atmospheric rivers and their implications for winter flooding in Britain *Envrion. Res. Lett.* 8 034010
- Ma J and Xie S-P 2013 Regional patterns of sea surface temperature change: a source of uncertainty in future projections of precipitation and atmospheric circulation *J. Clim.* **26** 2482–501
- Mizuta R, Yoshimura H, Murakami H, Matsueda M, Endo H, Ose T, Kamiguchi K *et al* 2012 Climate simulations using MRI-AGCM3.2 with 20-km grid *J. Meteorol. Soc. Japan* **90A** 233–58
- Mizuta R, Arakawa O, Ose T, Kusunoki S, Endo H and Kitoh A 2014 Classification of CMIP5 future climate responses by the tropical sea surface temperature changes *SOLA* **10** 167–71
- Mizuta R, Murata A, Ishii M, Shiogama H, Hibino K, Mori N, Arakawa O, Imada Y *et al* 2017 Over 5000 years of ensemble future climate simulations by 60-km global and 20-km regional atmospheric models *Bull. Am. Meteorol. Soc.* 98 1383–98
- Mundhenk B D, Barnes E A and Maloney E D 2016 All-season climatology and variability of atmospheric river frequencies over the North Pacific *J. Clim.* **29** 4885–903
- Neiman P J, Ralph F M, Moore B J, Hughes M, Mahoney K M,
 Cordeira J M and Dettinger M D 2013 The landfall and inland
 penetration of a flood-producing atmospheric river in
 Arizona: I. Observed synoptic-scale, orographic, and
 hydrometeorological characteristics *J. Hydrometeorol.* 14
 460–84
- O'Gorman P A, Allan R P, Byrne M P and Previdi M 2012 Energetic constraints on precipitation under climate change *Surv*. *Geophys.* 33 585–608
- Paek H, Yu J Y, Zheng F and Lu M M 2018 Impacts of ENSO diversity on the western Pacific and North Pacific subtropical highs during boreal summer *Clim. Dyn.* accepted (https://doi.org/10.1007/s00382-016-3288-z)
- Payne A E and Magnusdottir G 2015 An evaluation of atmospheric rivers over the North Pacific in CMIP5 and their response to warming under RCP 8.5 *J. Geophys. Res. Atmos.* **120** 11173–90
- Shepherd T G 2014 Atmospheric circulation as a source of uncertainty in climate change projections *Nat. Geosci.* 7 703–8
- Shields C A and Kiehl J T 2016 Atmospheric river landfall-latitude changes in future climate simulations *Geophys. Res. Lett.* 43 8775–82
- Shields C A et al 2018 Atmospheric river tracking method intercomparison project (ARTMIP): project goals and experimental design Geosci. Model Dev. 11 2455–74
- Shin S-I and Sardeshmukh P D 2011 Critical influence of the pattern of tropical ocean warming on remote climate trends *Clim. Dyn.* 36 1577–91
- Song F and Zhou T 2014a Interannual variability of East Asian summer monsoon simulated by CMIP3 and CMIP5 AGCMs: Skill dependence on Indian Ocean—western Pacific anticyclone teleconnection *J. Clim.* 27 1679–97
- Song F and Zhou T 2014b The climatology and interannual variability of East Asian summer monsoon in CMIP5 coupled models: Does air–sea coupling improve the simulations? *J. Clim.* 27 8761–77
- Song F, Leung L R, Lu J and Dong L 2018 Future changes in seasonality of the North Pacific and North Atlantic subtropical highs Geophys. Res. Lett. 45 11959–68



- Taylor K E, Stouffer R J and Meehl G A 2012 An overview of CMIP5 and the experiment design *Bull. Am. Meteorol. Soc.* **90** 485–98
- Thompson D W J, Barnes E A, Deser C, Foust W E and Phillips A 2015 Quantifying the role of internal climate variability in future climate trends *J. Clim.* **28** 6443–56
- Tsuguti H, Seino N, Kawase H, Imada Y, Nakaegawa T and Takayabu I 2019 Meteorological overview and mesoscale characteristics of the Heavy Rain Event of July 2018 in Japan *Landslides* 16 363–71
- Waliser D and Guan B 2017 Extreme winds and precipitation during landfall of atmospheric rivers *Nat. Geosci.* 10 179–83
- Wang B, Xiang B and Lee J-Y 2013 Subtropical high predictability establishes a promising way for monsoon and tropical storm predictions *Proc. Natl Acad. Sci. USA* 110 2718–22
- Warner M E, Mass C F and Salathé E P Jr 2015 Changes in winter atmospheric rivers along the North American west coast in CMIP5 climate models J. Hydrometeorol. 16 118–28

- Wick G A, Neiman P J, Ralph F M and Hamill T M 2013 Evaluation of forecasts of the water vapor signature of atmospheric rivers in operational numerical weather prediction models *Weather Forecast.* 28 1337–52
- Xie S-P, Hu K, Hafner J, Tokinaga H, Du Y, Huang G and Sampe T 2009 Indian Ocean capacitor effect on Indo-western Pacific climate during the summer following El Niño *J. Clim.* 22 730–47
- Xie S-P, Deser C, Vecchi G A, Ma J, Teng H and Wittergerg A T 2010 Global warming pattern formation: Sea surface temperature and rainfall *J. Clim.* 23 966–86
- Xie S-P *et al* 2015 Towards predictive understanding of regional climate change *Nat. Clim. Change* 5 921–30
- Xie S-P, Kosaka Y, Du Y, Hu K, Chowdary J S and Huang G 2016 Indo-western Pacific ocean capacitor and coherent climate anomalies in post-ENSO summer: a review *Adv. Atmos. Sci.* 33 411–32